HHS Public Access
Author manuscript
Proc SPIE Int Soc Opt Eng. Author manuscript; available in PMC 2014 October 07.

Published in final edited form as:
Proc SPIE Int Soc Opt Eng. 2014 March 21; 9034: 90342X–. doi:10.1117/12.2043282.

Interpolation of Longitudinal Shape and Image Data via Optimal Mass Transport

Yi Gao[a], **Liang-Jia Zhu**[b], **Sylvain Bouix**[c], and **Allen Tannenbaum**[b]

[a]Department of Electrical and Computer Engineering and the Comprehensive Cancer Center, the University of Alabama at Birmingham; 1150 10th Avenue South, Birmingham, AL 35294

[b]Departments of Computer Science and Applied Mathematics/Statistics, Stony Brook University, Stony Brook, New York, 11794

[c]Department of Psychiatry, Harvard Medical School, 1249 Boylston St, Boston, MA, 02215

Abstract

Longitudinal analysis of medical imaging data has become central to the study of many disorders. Unfortunately, various constraints (study design, patient availability, technological limitations) restrict the acquisition of data to only a few time points, limiting the study of continuous disease/treatment progression. Having the ability to produce a sensible time interpolation of the data can lead to improved analysis, such as intuitive visualizations of anatomical changes, or the creation of more samples to improve statistical analysis. In this work, we model interpolation of medical image data, in particular shape data, using the theory of optimal mass transport (OMT), which can construct a continuous transition from two time points while preserving “mass” (e.g., image intensity, shape volume) during the transition. The theory even allows a short extrapolation in time and may help predict short-term treatment impact or disease progression on anatomical structure. We apply the proposed method to the hippocampus-amygdala complex in schizophrenia, the heart in atrial fibrillation, and full head MR images in traumatic brain injury.

1. Description of Purpose

In most longitudinal study design of medical imaging, the temporal resolution is very coarse. For example, one might scan a schizophrenic patient at the first psychotic episode, a year later and yet a few years later at the chronic stage. The reasons for this coarse sampling are numerous, stemming from the difficulty of following study subjects regularly, the cost of acquiring images, or the risk of radiation exposure. While the exact information between time point is not known, we propose in this paper a formulation to interpolate imaging data from existing samples in order to provide a more continuous view of a disease/treatment progression.

While longitudinal shape and image analysis have been extensively studied,[1–9] shape and image are often treated differently and few methods provide temporal interpolation.[10–13] In this work, we propose a general framework using optimal mass transport (OMT) theory to extract diffeomorphic mapping and interpolate shapes and images through this mapping. OMT has been used in the context of image registration,[14] although the strong constraint of “mass” preservation (i.e. image intensity) can be problematic when registering images from different subjects. In contrast, in shape analysis or mesh generation,[15] preserving mass (i.e. volume) between time points is a desirable feature, and OMT is well suited for this application. This is also true between images of the same subject at different time points, provided image changes are not drastic. In addition to performing "interpolation" between discrete time points, the proposed framework can also "extrapolate", for a short time, beyond the last time point (OMT was used to study the evolution of the early universe[16]), providing short-term predictions of disease/treatment progression.

2. Method

2.1 OMT formulation

Originally formalized by the French civil engineer Gaspard Monge in 1781 and given a modern measure-theoretic formulation by Kantorovich in 1948, the OMT problem has now become used in a wide range of field including geometry, economics, shape optimization, probability theory, control, statistics, and imaging science. See[17] and the many references therein for extensive treatments. It is also noted that the discrete model of OMT has also been employed,[18,19] however, in this work we adopt the continuous formulation, which is briefly described below.

Let Ω_0 and Ω_1 be two diffeomorphic subdomains of $\mathbb{R}^d$ with smooth boundaries, each equipped with a positive density function, μ_0 and μ_1, respectively, and which satisfy the "equal total mass requirement": $\int_{\Omega_0}\mu_0(\boldsymbol{x})d\boldsymbol{x}=\int_{\Omega_1}\mu_1(\boldsymbol{x})d\boldsymbol{x}$. We call a diffeomorphism $\boldsymbol{u}$: $\Omega_0\to\Omega_1$ *mass preserving* (MP) if $\int_{u^{-1}(D)}\mu_0(\xi)d\xi=\int_D\mu_1(\boldsymbol{x})d\boldsymbol{x},\forall D\subseteq\Omega_1$, with $\mathbf{x} = \mathbf{u}(\xi)$. Via change of variables, this can be rewritten as $\det(J(\boldsymbol{u}(\boldsymbol{x})))\mu_1(\boldsymbol{u}(\boldsymbol{x})) = \mu_0(\boldsymbol{x}),\forall \boldsymbol{x}\in\Omega_0$ where $J(\boldsymbol{u}(\boldsymbol{x}))$ is the Jacobian of $\boldsymbol{u}$ at $\boldsymbol{x}$. This is referred to as the *Jacobian equation*. The latter equation is highly nonlinear, and may have many solutions. The objective of OMT is to compute the following distance and find the corresponding optimal transportation map (if it exists), defined in terms of the L^p Kantorovich-Wasserstein functional:

$$d_p(\mu_0,\mu_1)^p=\inf_{\boldsymbol{u}\in MP}\left(\int_\Omega|\boldsymbol{u}(\boldsymbol{x})-\boldsymbol{x}|^p\mu_0(\boldsymbol{x})d\boldsymbol{x}\right). \quad (1)$$

The quadratic version of this problem *(p = 2* in Eq.(1)) has been extensively studied, and in this case one can show that there exists a unique convex function $\tilde{\Psi}:\Omega\to\Omega$ such that the optimal mapping $\tilde{\boldsymbol{u}}$ is the gradient of $\tilde{\Psi}$, i.e., $\tilde{\boldsymbol{u}}=\nabla\tilde{\Psi}$.[20] The MK problem for $p = 2$ has a number of approaches devoted to its numerical solution; see[14,18,21,22] and the references therein. In this study, we use the method recently developed by Haber *et al.* which expresses Eq. (1) as a variational problem solved via sequential quadratic programming.[23] From now on, OMT will refer to the L^2 Monge-Kantorovich problem. One particular important feature of OMT is that its inverse transformation can be computed analytically. In fact, the inverse transformation $\tilde{\boldsymbol{u}}^{-1}(\boldsymbol{x})$ it is given by the gradient of the convex function Θ via $\tilde{\boldsymbol{u}}^{-1}(\boldsymbol{x})=\nabla_{\boldsymbol{x}}\Theta(\boldsymbol{x})=\max_{\boldsymbol{q}}[\boldsymbol{q}\cdot\boldsymbol{x}-\tilde{\Psi}(\boldsymbol{q})]$. Finally, since we will be dealing with images and 3D shapes, for simplicity we will take $\Omega_0 = \Omega 1 = \mathbb{R}^d$ (d = 2, 3) in the sequel, since anyway the densities will always have compact support.

2.2 Longitudinal interpolation of image and shape analysis

Given two images scanned at two distinct time points $t = T_0$ and $t = T_1 (> T_0)$, we aim to generate image samples at times $t \in [T_0, T_1]$ by first solving the OMT for the two images, and then use the resulting transport mapping to interpolate between the samples. First, we define the densities as the normalized intensities of the images $\mu_0 := I(\boldsymbol{x}, T_0)/\|I(T_0)\|_2$ and $\mu_1 := I(\boldsymbol{x}, T_1)/\|I(T_1)\|_2$. Then the optimal transport mapping $\tilde{\boldsymbol{u}}$ is computed by minimizing the Kantorovich-Wasserstein functional equation (1) via the method given in.[23]

Furthermore, setting $\boldsymbol{v} := (\tilde{\boldsymbol{u}}(\boldsymbol{x}) - x)/(T_1 - T_0)$, define $\boldsymbol{w} : \mathbb{R}^d \times [T_0, T_1] \to \mathbb{R}^d : \boldsymbol{w}(\boldsymbol{x}, t) := \boldsymbol{x} + (t - T_0)\boldsymbol{v}$ and then define the image sequence:

$$I(\boldsymbol{x}, t) := \det(J(\boldsymbol{w}(\boldsymbol{x}, t)))\mu_0(\boldsymbol{w}(\boldsymbol{x}, t)). \quad (2)$$

Note that $I(\boldsymbol{x}, t)|_{t=T_0} = \mu_0(\boldsymbol{x})$ and $I(\boldsymbol{x}, t)|_{t=T_1} = \mu_1(\boldsymbol{x})$. Hence, a smooth evolution trajectory is reconstructed from T_0 to T_1. It turns out from the results of,[22,24] the sequence defined in (2) gives the optimal warp (elastic deformation) from μ_0 to μ_1 in the OMT sense. Indeed, it defines a geodesic path in the space of densities with respect to the Wasserstein 2-metric.[17,25] The Wasserstein metric imparts a natural Riemannian structure to the space of densities.

In addition, such reconstructions can be extrapolated (slightly) into the future since the property of being a diffeomorphism is an open condition. More precisely, by letting t go beyond T_1, we obtain the estimated density at time after the scan time T_1. Note that since $\boldsymbol{u}$ is diffeomorphism, so is $\boldsymbol{w}$ for all $t \in [T_0, T_1]$. However, for $t > T_1$, the diffeomorphic property of $\boldsymbol{w}$ may only exist for a small increment, i.e., for $t \in [T_0, T_1 + \varepsilon]$. As a result, the prediction into the future can only be performed for a relative short periods.

One particularly interesting application is the interpolation of shape structures. The image $I(\boldsymbol{x})$ above can also be a binary volume representation of an anatomical shape, and statistical shape analysis can then be "interpolated" to any time point between T_0 and T_1. More explicitly, denote a set of shapes at times T_0 and T_1 as $\check{I}_1^A(\boldsymbol{x}, T_0), \ldots, \check{I}_M^A(\boldsymbol{x}, T_0)$ and $\check{I}_1^A(\boldsymbol{x}, T_1), \ldots, \check{I}_M^A(\boldsymbol{x}, T_1) : \mathbb{R}^3 \to \{0, 1\}$. Similarly, denote a second group of shapes as $\check{I}_1^B(\boldsymbol{x}, T_0), \ldots, \check{I}_N^B(\boldsymbol{x}, T_0)$ and $\check{I}_1^B(\boldsymbol{x}, T_1), \ldots, \check{I}_N^B(\boldsymbol{x}, T_1) : \mathbb{R}^3 \to \{0, 1\}$. Note that M can be different from N.

Using the optimal mass transport, a continuous shape trajectory between T_0 and T_1 can be computed as $\check{I}_i^j : \mathbb{R}^3 \times [T_0, T_1] \to [0, 1]$. Then, at time $t \in [T_0, T_1]$, in order to compute the regions where the two groups are statistically different, we first register the two groups $\check{I}_1^A(\boldsymbol{x}, t), \ldots, \check{I}_M^A(\boldsymbol{x}, t)$ and $\check{I}_1^B(\boldsymbol{x}, t), \ldots, \check{I}_N^B(\boldsymbol{x}, t)$. This can be done by arbitrarily picking one of the shapes, $\check{I}$ and registering all the others to it by minimizing the energy $E(\mathscr{A}_i^j)$ with respect to each similarity transformation $\mathscr{A}_i^j : \mathbb{R}^3 \to \mathbb{R}^3$, where $E(\mathscr{A}_i^j)$ is defined as $E(\mathscr{A}_i^j) := \int_\Omega \left(\check{I}_i^j(\mathscr{A}_i^j \circ \boldsymbol{x}, t) - \check{I}(\boldsymbol{x}, t)\right)^2 \mathrm{d}\boldsymbol{x}, j \in \{A, B\}, i \in \{1, \ldots, M \text{ or } N\}$. After registration, we denote the registered shapes as $I_1^A(\boldsymbol{x},t),\ldots,I_M^A(\boldsymbol{x},t)$ and $I_1^B(\boldsymbol{x},t),\ldots,I_N^B(\boldsymbol{x},t)$. The mean shape $M:\mathbb{R}^3\times[T_0,T_1]\to[0,1]$ is then computed simply as the arithmetic average of $I_1^A(\boldsymbol{x},t),\ldots,I_M^A(\boldsymbol{x},t)$ and $I_1^B(\boldsymbol{x},t),\ldots,I_N^B(\boldsymbol{x},t)$. Correspondingly the mean shape surface $S(t)\subset\mathbb{R}^3$ is computed as the 0.5-isosurface of $M(\boldsymbol{x}, t)$.

In parallel, for each of the registered shapes, I_i^j's, a signed distance function $D_i^j:\mathbb{R}^3\times[T_0,T_1]\to\mathbb{R}$ is constructed as:

$$D_i^j(\boldsymbol{x},t)=\begin{cases}\inf_{\boldsymbol{y}\in S}\|\boldsymbol{x}-\boldsymbol{y}\|_2, & \text{if } I_i^j(\boldsymbol{x},t)\le 0.5\\ -\inf_{\boldsymbol{y}\in S}\|\boldsymbol{x}-\boldsymbol{y}\|_2, & \text{if } I_i^j(\boldsymbol{x},t)>0.5\end{cases}\qquad j\in\{A,B\},i\in\{1,\ldots,M\text{ or }N\} \tag{3}$$

At this point, all the shapes can be converted to scalar functions defined on the same domain S by restricting D_i^j's to S. Then, for each point s on$S$, two groups of numbers $\left\{D_i^A(s)\right\}$ and $\left\{D_i^B(s)\right\}$ can be extracted. Under the null hypothesis that the means of the two groups are the same, we perform the student t-test, and the corresponding p-value is recorded for the point s. Due to the fact that the t-test is performed multiple times, the multiple comparison effect is corrected using the false discovery rate algorithm.[26] The final corrected p-values give a scalar p- value map $P : S \times [T_0, T_1] \to [0, 1]$ defined on the mean shape surface.

3. Results

3.1 Longitudinal shape analysis in schizophrenia

We applied our technique to a set of amygdala hippocampal complex (AHC) manual segmentations outlined from T1 weighted MR images, acquired in patients with schizophrenia and matched controls. 17 normal subjects and 17 patients are studied where the patients were evaluated at first episode and scanned thirteen months later to study the disease progression. The results of the analysis are shown in Figure 1(a), where the numbers in subfigures indicate the time variable. Note that only the shapes at time 0 and 1 are obtained from MR images. All the others are computed using the proposed method. From Figure 1(a). we can see that the significantly different regions gradually change their locations as time elapses. This may be correlated with the disease progression and provide some useful information to the physicians.

3.2 Longitudinal shape analysis for the atrial fibrillation patients

Among patients who undergo radio-frequency ablation treatment for left atrial fibrillation (AFib), a significant number (variously estimated to be about 30%) have AFib recurrence.[27] 21 cured patients and 11 patients with AFib recurrence were scanned (late gadolinium enhanced MR imaging) pre-ablation and three months postablation. Studying the shapes of the left atrium of the cured patients versus the recurrent patients reveals the significantly different regions shown by the colormap in Figure 1(b). The proposed method provides a continuous profile between the two time points (pre-ablation and post-ablation).

3.3 Traumatic brain injury (TBI) image study

In Figure 2, only times 0 and 1 are real FLAIR MR images, and all the others are computed using the proposed method. The injured region is indicated by the arrow. The healing process is better illustrated with the gradual progression provided by OMT, rather than with only the two physically acquired images. In the bottom-right corner, we predict the image in the near future. It can be seen that the dark edema region is getting larger. This could provide a useful suggestion for the physicians for future treatment. It is also noted that the test is performed in 3D but only the axial view is shown for clarity.

4. Conclusion and New Work to be Presented

OMT leads to a natural Riemannian metric on the space of images and shapes as described in this work. Since the geodesic paths are easy to compute once one has the optimal transport map, one can derive a simple method of interpolating shapes and images. This observation is the basis of our technique for longitudinal analysis. Indeed, using OMT, we have indicated how we may provide a dynamical approach for longitudinal image and shape analysis. The method is applied in the context of shape analysis and image interpolation. In continuous disease progression, the interpolation might provide a very realistic approximation of the actual biological phenomenon, although this needs to be further validated. A number of future directions could lead to some very interesting work. For example one could generate a dense temporal sampling of shapes and “normalize” acquisition time via spatiotemporal registration. Another application would be to incorporate tissue density as a shape feature and use OMT to create a mapping taking this “density” into account. Moreover, we plan to incorporate biological evolution rules into the OMT framework to attempt to better model disease progression for the three scenarios considered in this work. We also plan to use OMT for the modeling of cancer tumor growth. Indeed, the continuous models derived via OMT may be useful in setting certain parameters of various differential equation models of tumor progression, which up until now had to rely on a small number of images taken at several widely separated time intervals.

References

1. Gerig, G.; Styner, M.; Jones, D.; Weinberger, D.; Lieberman, J. IEEE MMBIA. IEEE; 2001. Shape analysis of brain ventricles using spharm; p. 171-178.
2. Cates J, Fletcher P, Styner M, Hazlett H, Whitaker R. Particle-based shape analysis of multiobject complexes. MICCAI. 2008:477–485. [PubMed: 18979781]
3. Shen L, Farid H, McPeek M. Modeling three-dimensional morphological structures using spherical harmonics. Evolution. 2009; 63(4):1003–1016. [PubMed: 19154365]
4. Ashburner J, Friston K. Voxel-based morphometry–the methods. Neuroimage. 2000; 11(6):805–821. [PubMed: 10860804]
5. Styner M, Gerig G, Lieberman J, Jones D, Weinberger D. Statistical shape analysis of neuroanatomical structures based on medial models. Medical Image Analysis. 2003; 7(3):207–220. [PubMed: 12946464]
6. Miller M. Computational anatomy: shape, growth, and atrophy comparison via diffeomorphisms. NeuroImage. 2004; 23:S19–S33. [PubMed: 15501089]
7. Heimann T, Meinzer H. Statistical shape models for 3d medical image segmentation: A review. Medical image analysis. 2009; 13(4):543–563. [PubMed: 19525140]

8. Gao Y, Corn B, Schifter D, Tannenbaum A. Multiscale 3D shape representation and segmentation with applications to hippocampal/caudate extraction from brain MRI. Medical Image Analysis. 2012; 16(2):374–385. [PubMed: 22119491]
9. Gao Y, Bouix S. Synthesis of realistic subcortical anatomy with known surface deformations. MICCAI Workshop on Mesh Processing in Medical Image Analysis. 2012:80–88.
10. Durrleman S, Pennec X, Trouvè A, Braga J, Gerig G, Ayache N. Towards a comprehensive framework for the spatiotemporal statistical analysis of longitudinal shape data. IJCV. 2012:1–38.
11. Fishbaugh J, Prastawa M, Durrleman S, Piven J, Gerig G. Analysis of longitudinal shape variability via subject specific growth modeling. MICCAI. 2012:731–738. [PubMed: 23285617]
12. Hong Y, Joshi S, Sanchez M, Styner M, Niethammer M. Metamorphic geodesic regression. MICCAI. 2012
13. Xu S, Zhu H, Styner M, Gao W, Jewells V, Shen D, Lin W. Longitudinal shape analysis of lateral ventricles during the first year of human life. ISMRM. 2011
14. Haker S, Zhu L, Tannenbaum A, Angenent S. Optimal mass transport for registration and warping. IJCV. 2004; 60(3):225–240.
15. Sandhu, R.; Dominitz, A.; Gao, Y.; Tannenbaum, A. Volumetric mapping of genus zero objects via mass preservation. 2012. arxiv.org/abs/1205.1225
16. Frisch U, Matarrese S, Mohayaee R, Sobolevski A. A reconstruction of the initial conditions of the universe by optimal mass transportation. Nature. 2002; 417:260–262. [PubMed: 12015595]
17. Villani, C. Optimal Transport: Old and New. Vol. 338. Springer; 2008.
18. Wang W, Ozolek JA, Slepcev D, Lee AB, Chen C, Rohde GK. An optimal transportation approach for nuclear structure-based pathology. IEEE TMI. 2011; 30(3):621–631.
19. Wang W, Slepčev D, Basu S, Ozolek JA, Rohde GK. A linear optimal transportation framework for quantifying and visualizing variations in sets of images. IJCV. 2013; 101(2):254–269.
20. Brenier Y. Polar factorization and monotone rearrangement of vector-valued functions. Comm on pure and applied mathematics. 1991; 44(4):375–417.
21. Kaijser T. Computing the Kantorovich distance for images. JMIV. 1998; 9(2):173–191.
22. Benamou J, Brenier Y. A computational fluid mechanics solution to the Monge-Kantorovich mass transfer problem. Numerische Mathematik. 2000; 84(3):375–393.
23. Haber E, Rehman T, Tannenbaum A. An efficient numerical method for the solution of the l2 optimal mass transfer problem. SIAM Journal on Imaging Science. 2010; 32(1):197–211.
24. Gangbo W, McCann R. The geometry of optimal transportation. Acta Mathematica. 1996; 177(2): 113–161.
25. Jordan R, Kinderlehrer D, Otto F. The variational formulation of the fokker-planck equation. SIAM J Math Anal. 1998; 29:1–17.
26. Benjamini Y, Hochberg Y. Controlling the false discovery rate: a practical and powerful approach to multiple testing. Journal of the Royal Statistical Society Series B. 1995:289–300.
27. Balk E, Garlitski A, Alsheikh-Ali A, Terasawa T, Chung M, Ip S. Predictors of atrial fibrillation recurrence after radiofrequency catheter ablation: a systematic review. Journal of Cardiovascular Electrophysiology. 2010; 21(11):1208–1216. [PubMed: 20487117]

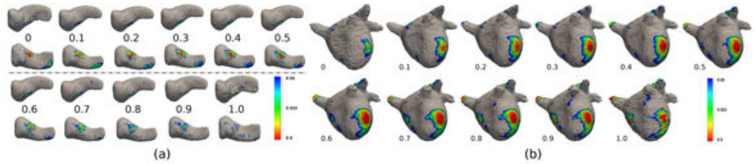

Figure 1.

The gray color indicates those regions that are not significantly different between: (a) healthy and schizophrenia subjects and (b) cured and recurrent AFib patients. The red color indicates regions that are significantly different between the two groups.

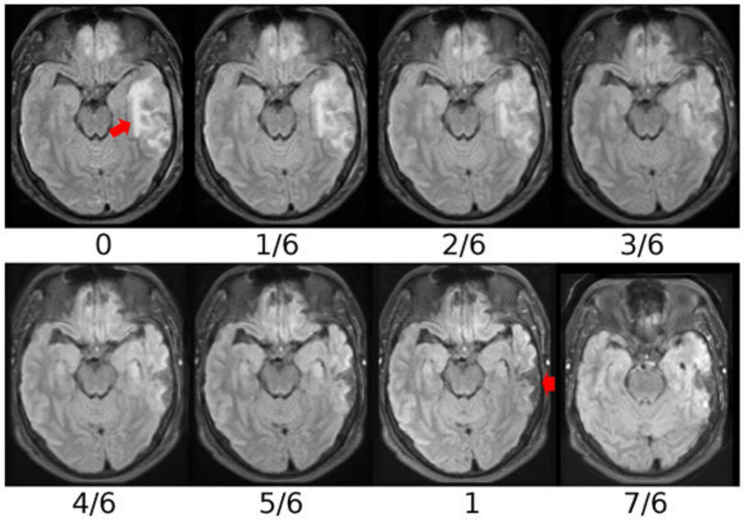

Figure 2.

Healing of TBI. The number below each image indicates "time." Only times 0 and 1 are real images, and all the others are computed using the proposed OMT method. The healing process of the injured region pointed to the arrow is better illustrated by the gradual progression than simply having the two original images at time 0 and 1. The prediction in the near future is shown on the bottom-right.